

Article

Research on Soft Flutter of 420m-Span Pedestrian Suspension Bridge and Its Aerodynamic Measures

Qinghai Guan ^{1,*} , Lei Liu ², Hui Gao ^{3,*}, Yujing Wang ¹ and Jiawu Li ⁴¹ School of Transportation Engineering, Shandong Jianzhu University, Jinan 250101, China² Tianjin Key Laboratory of Civil Structure Protection and Reinforcement, Tianjin Chengjian University, Tianjin 300384, China³ Department of Civil Engineering, Ordos Institute of Technology, Ordos 017000, China⁴ Wind Tunnel Laboratory, Chang'an University, Xi'an 710064, China

* Correspondence: 14017@sdjzu.edu.cn (Q.G.); gh@oit.edu.cn (H.G.)

Abstract: In order to study the flutter of long-span pedestrian suspension bridge and its aerodynamic control, a 420m-span pedestrian suspension bridge is used as an engineering example, the wind-induced vibration of seven particular aerodynamic sections is studied by wind tunnel tests, and the soft flutter phenomenon of two kinds of aerodynamic sections is identified. The results show that the wind fairing and the wind-retaining plate measures are not necessarily effective measures to improve the wind-induced stability of long-span pedestrian suspension bridge, as these two measures may reduce the flutter stability: the wind fairing section in the positive angle of attack is prone to torsion-based soft flutter phenomenon, in which the vertical vibration spectrum contains multiple vibration frequencies, so the conventional formulation of the linearized self-excited forces is no longer satisfied; the wind-retaining plate section in the negative angle of attack is prone to soft flutter dominated by vertical vibration, and the beat vibration phenomenon is found in the torsional vibration time history of the wind-retaining section. Slotting in the center of the girder section can significantly change the flow state of the section, which is an effective measure to improve the flutter stability of the pedestrian suspension bridge.

Keywords: aerodynamic measure; long-span pedestrian suspension bridge; soft flutter identification; wind tunnel test



Citation: Guan, Q.; Liu, L.; Gao, H.; Wang, Y.; Li, J. Research on Soft Flutter of 420m-Span Pedestrian Suspension Bridge and Its Aerodynamic Measures. *Buildings* **2022**, *12*, 1173. <https://doi.org/10.3390/buildings12081173>

Academic Editors: Minshui Huang and Jianfeng Gu

Received: 28 June 2022

Accepted: 3 August 2022

Published: 5 August 2022

Publisher's Note: MDPI stays neutral with regard to jurisdictional claims in published maps and institutional affiliations.



Copyright: © 2022 by the authors. Licensee MDPI, Basel, Switzerland. This article is an open access article distributed under the terms and conditions of the Creative Commons Attribution (CC BY) license (<https://creativecommons.org/licenses/by/4.0/>).

1. Introduction

In recent years, China has built many long-span pedestrian suspension bridges, most of which are located in scenic areas and span deep canyons [1–4]. Long-span pedestrian suspension bridges with low stiffness girder are prone to dynamic stability problems, and the factors causing dynamic instability are mainly pedestrians and wind loads. The most famous case of dynamic instability caused by pedestrians is the Millennium Bridge in London in 2000 [5,6]. Cases of human-induced instability have occurred in many pedestrian bridges and have attracted the full attention of bridge design engineers [7–9].

On the other hand, many long-span pedestrian suspension bridges across deep canyons are susceptible to canyon wind effects and become wind-sensitive structures, so it is especially important to study the wind-induced vibration and instability of the pedestrian suspension bridges, and their aerodynamic control. Bridge wind-induced vibration mainly includes two types of self-limiting vibration (buffeting and vortex-induced vibration), and self-excited divergence vibration (flutter and galloping). The wind-induced instability of bridges is caused by the action of wind, which can be divided into aerostatic instability and aerodynamic instability, where the bridge aerodynamic instability mainly includes flutter and galloping. Many efforts have been made to investigate the wind-induced vibration and instability of the pedestrian suspension bridges by wind tunnel tests and numerical simulations, and some research results have been obtained. In the early years,

some experts and scholars studied the aeroelastic characteristics and wind-induced vibrations of the stressed ribbon pedestrian bridge [10,11]. Stoyanoff [12] proposed a general quasi-steady approach for evaluation of 3D galloping stability and buffeting response, and the galloping stability analysis was verified on the I235 Pedestrian Bridge, Iowa. Through the case studies of a long-span suspension bridge and a light suspension footbridge, Salvatori and Spinelli [13] observed that structural nonlinearities deemphasize the presence of a critical flutter wind velocity, as they limit the oscillation amplitudes. By the flutter investigation and the proper orthogonal decomposition (POD) analysis, Taylor et al. [14,15] highlighted the strong influence of the pedestrian barriers on the overall aerodynamic characteristics and aeroelastic stability of the bridge. Rizzo et al. [16] analyzed three different experimental data sets measured in three different wind tunnel laboratories, and found that experimental error propagation, associated with variability in the aerodynamic loads of bridge decks, has considerable impact on the critical flutter speed of pedestrian suspension bridges. Lebedev et al. [17] investigated the aerodynamic characteristics of the fiber reinforcement plastic (FRP) pedestrian suspension bridge and found that perforation of the sides of lower beams and railings can be considered a very effective way of suppression vortex induced vibrations. Salenko et al. [18] further studied the strength, flexural rigidity, and aerodynamic stability of the FRP pedestrian suspension bridge. It was verified by wind tunnel tests that utilizing decorative wind chimes can provide stabilization effects against flutter instability [19]. Qi et al. [20] proposed a new-style cable net structure consisting of a wind-resistance main cable, wind-resistance secondary cable, and pulleys to improve the wind-resistance stability of pedestrian suspension bridge. Using computational fluid dynamics (CFD) and wind tunnel tests, Tadeu et al. [21] analyzed the aerodynamic performance of a long-span suspension bridge, the 516 Arouca bridge with a span length of 516.5 m, in a hilly location in Portugal.

However, there are still the following issues which need to be considered.

(1) Compared with vehicular suspension bridge, pedestrian suspension bridge has smaller structural mass and lower stiffness, which is easier to cause wind-induced vibration. Moreover, most of the girders of long-span pedestrian suspension bridges are typical bluff body structures. The flutter characteristics of such girder structures need to be studied in detail, which may differ greatly from that of vehicle bridges.

(2) Most of the existing wind resistance studies of pedestrian bridges are case studies, and the research conclusions are often limited to specific bridges, which is difficult to be fully extended to other pedestrian bridges, so a general pedestrian suspension bridge case study is needed.

(3) Much research has found that a slot at the center of a girder can improve the aerodynamic stability [22–25]. Tang et al. [26] found that the existence of central slot can improve the critical flutter wind velocity at lower angles of attack, however, the existence of central slot further decreases the flutter performance at larger angles of attack. It is found that a reasonable type of wind fairings could improve the flutter performance and suppress the vortex-induced vibration of long-span bridges [27,28]. It is necessary to further study whether the measures such as wind fairing and central slot are necessarily effective for the pedestrian suspension bridge girder section. The suitable aerodynamic measures for the pedestrian suspension bridge girder need to be clarified and the wind-induced instability problems of different measures need to be analyzed.

In this study, seven particular aerodynamic design sections are proposed based on the structural characteristics of the girder of a 420m-span pedestrian suspension bridge in China. A combination of wind tunnel tests and numerical simulations is used to study the flutter response, to investigate the flutter characteristics, and to analyze the suitable aerodynamic measures for the pedestrian suspension bridge girder. The present study can also provide reference for the wind resistance design of long-span pedestrian suspension bridges.

2. Descriptions of the Tianmeng Bridge

Tianmeng Bridge is located at Tianmeng Tourism in Fei County, Linyi City, Shandong Province, China, and was completed and put into use in 2016, which is one of the world's largest spans of pedestrian suspension bridge. The photo of the bridge is shown in Figure 1.



Figure 1. Tianmeng Bridge in Shandong province, China.

The bridge span arrangement is (38 + 420 + 47.5) meters, concrete tower height is 39 m, two main cables center distance is 3.5 m, a total of 139 pairs of boom, boom spacing 3 m. The bridge is across the deep canyon, and the maximum height of the bridge from the valley floor is 143 m (see Figure 2a).

In order to improve the structural stability of the girder, two wind-resistant cables are set up on both sides of the girder. The average horizontal inclination of the wind-resistant cable is 45° , and each wind-resistant cable is composed of 7 galvanized steel ropes with nominal diameter of 56 mm. The spacing of wind-resistant hanger is 6 m, and a total of 57 wind-resistant hangers are arranged (see Figure 2b).

Compared with the girder of vehicular suspension bridge, the girder of pedestrian suspension bridge is smaller in size, smaller in width span ratio, and lighter in weight. The girder width is 4 m, and the width-to-span ratio of the girder section is 1:105. The girder is a typical bluff body with thin plate-truss, and the standard cross section of the girder is shown in Figure 2c. The girder structure consists of lower crossbeams, upper longitudinal beams, and cross braces. The crossbeams are made of Q345D 28b I-beams. Two overhaul rails made of 20b I-beams are added at the bottom of the girder. Four longitudinal beams are set above the crossbeams, and the longitudinal beams are made of Q345D 20b I-beams. 3000 mm \times 800 mm concrete slabs are mounted on the steel longitudinal beams. The railing columns are made of 1.75 m square steel tubes. The porosity of the railing meshwork is about 70%.

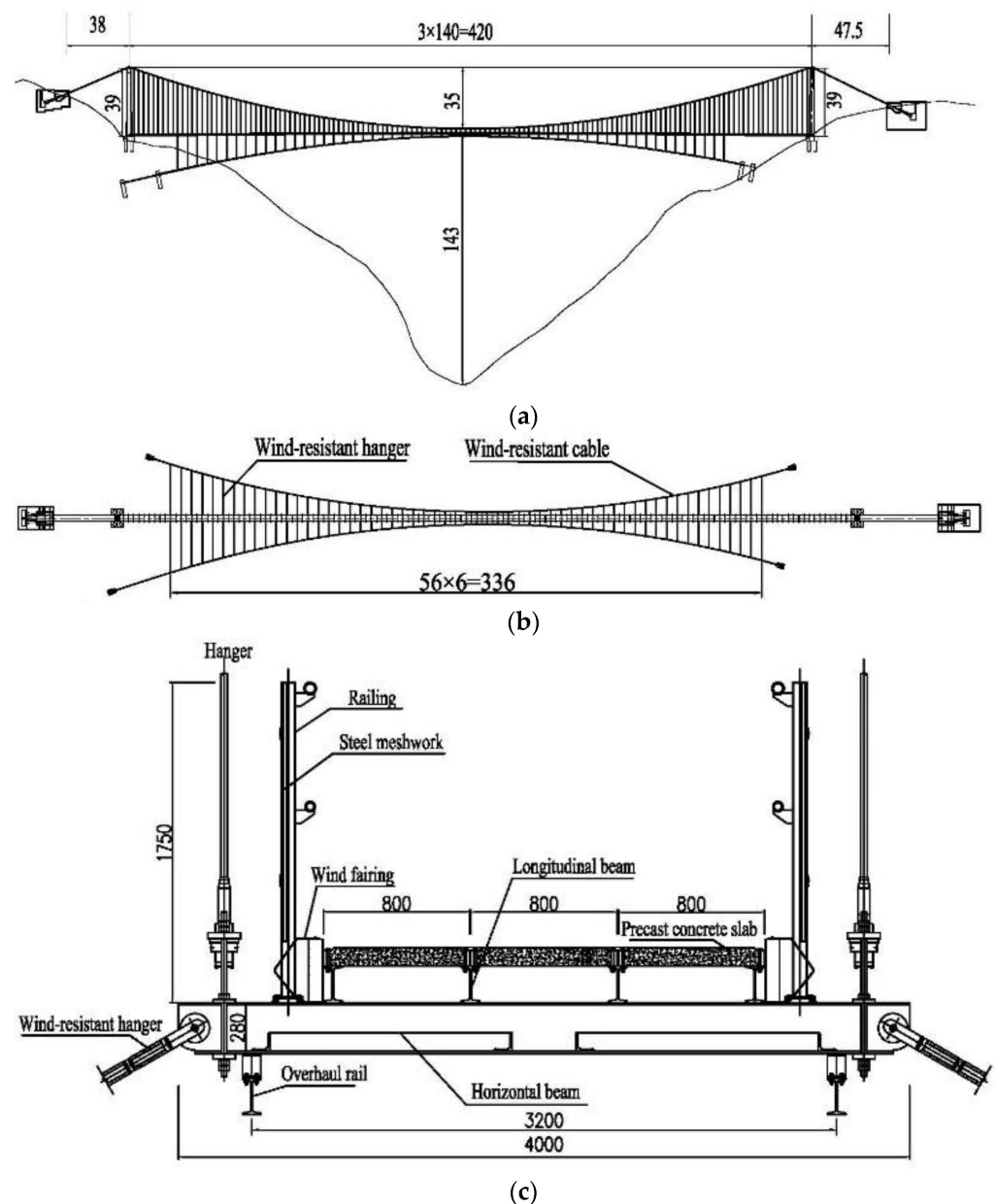


Figure 2. Configurations of the Tianmeng Bridge: (a) Elevation (m); (b) Deck level plan (m); (c) Girder cross section (mm).

3. Bridge Dynamic Characteristics and Wind Tunnel Tests

3.1. Main Structural Parameters and Finite Element Analysis (FEA) Model

The main structural parameters of the bridge are shown in Table 1. The densities of the cable members (include main cable, hanger, wind-resistant cable, and wind-resistant hanger) have been modified to account for the additional mass of the PE pipes. Steel Poisson's ratio is taken as 0.31, concrete Poisson's ratio is taken as 0.20.

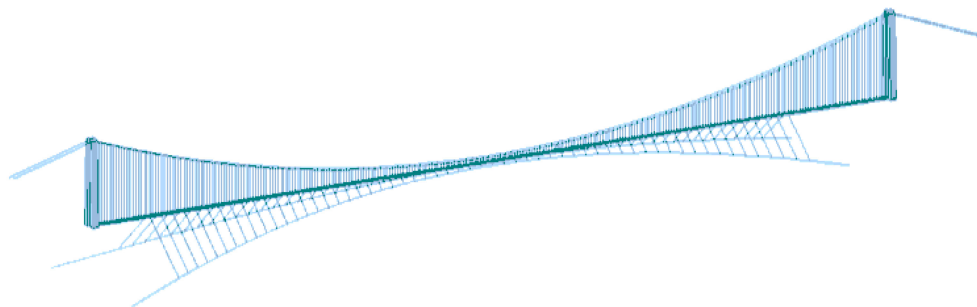
Table 1. Main structural parameters of the bridge.

Structural Components	Density (kg/m ³)	Area (m ²)	Elastic Modulus (N/m ²)	Vertical Bending MOI (m ⁴)	Lateral Bending MOI (m ⁴)	Torsion MOI (m ⁴)
longitudinal beam	7850	3.96×10^{-3}	2.06×10^{11}	2.50×10^{-5}	1.69×10^{-6}	1.47×10^{-7}
horizontal beam	7850	6.10×10^{-3}	2.06×10^{11}	7.48×10^{-5}	3.79×10^{-6}	3.15×10^{-7}
X-shape brace	7850	2.28×10^{-3}	2.06×10^{11}	2.09×10^{-6}	2.09×10^{-6}	1.08×10^{-7}
pylon	2550	6.0~3.0	3.45×10^{10}	4.5~1.0	2.0~0.56	4.73~1.26
main cable	8007	2.16×10^{-2}	2.00×10^{11}	-	-	-
wind-resistant cable	6903	1.38×10^{-2}	1.10×10^{11}	-	-	-

The general FEA software ANSYS Student 17.2 is used to model the bridge structure, and the overall coordinate system of the finite element model takes the longitudinal bridge direction as the X axis, the lateral bridge direction as the Z axis and the vertical bridge direction as the Y axis.

Cable structure has an obvious sag effect, which will affect the dynamic characteristics of the bridge structure. In order to consider the cable sag effect, some scholars use refined modeling strategies [29,30], and some use simplified schematization consistent with the Ernst's modulus [31,32]. In the present study, the Ernst equivalent modulus is used to account for the sag effect of cables. The main cable, hanger, wind-resistant cable, and wind-resistant hanger are simulated by 3D link element; the longitudinal beam, crossbeam, tower and other beam structures are discretized as 3D beam element; the accessory mass such as railing, concrete slab and cable clamp are simulated by nodal mass element.

The restraint conditions of the FEA model are: the bottom of the tower and the cable anchor are fixed restraints; and the main cable and the tower are coupled restraints at the top of the tower; the longitudinal displacement and torsional displacement at the end of the girder are free, and the vertical displacement is constrained. According to the structural mechanical properties of the bridge, the finite element model is established. The FEA model of the bridge is shown in Figure 3.

**Figure 3.** FEA model of the bridge.

3.2. Bridge Dynamic Characteristics

The equivalent mass and the equivalent mass moment of inertia (MOI) of the girder considering the full bridge vibration effects should be used in the mass system of the wind tunnel section model [33]. The equivalent mass and the equivalent mass MOI of the girder can be expressed as:

$$m_{eq}^d = \int_{L_g} \tilde{M} \varphi_d^2(x) dx \quad (1)$$

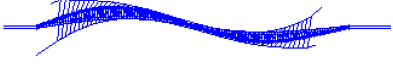
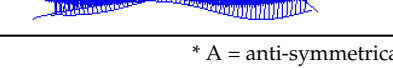
$$J_{meq}^x = \int_{L_g} \tilde{M} \varphi_{\theta_x}^2(x) dx \quad (2)$$

where m_{eq}^d , J_{meq}^x are the equivalent mass and the equivalent mass MOI of the girder per unit length in the modal sense, respectively; the superscript d represents the axis direction x , y and z ; \tilde{M} is the generalized modal mass of each order of eigenmode; $\varphi_d(x)$ is the d -direction

modal displacement of each order of eigenmode, and the subscript d represents the axis direction x , y and z , $\varphi_{\theta x}(x)$ is the torsion modal displacement of each order of eigenmode; L_g is the full length of the girder.

The Block Lanczos method is used for the modal analysis of the bridge, where the dynamic characteristics of some key modes are shown in Table 2.

Table 2. Dynamic characteristics of some key modes of the bridge.

Mode No.	Mode Shape	Mode of Vibration *	Frequency f (Hz)	Vertical Equivalent Mass (t/m)	Torsional Equivalent Mass MOI ($t \cdot m^2/m$)
1		A-L-1	0.235	273.5	620.6
2		S-L-1	0.237	2168	367.1
3		A-V-1	0.258	1.907	14360
5		S-V-1	0.335	2.135	27020
11		A-T-1	0.502	70.36	5.581

* A = anti-symmetrical; S = symmetrical; L = lateral; T = torsional; V = vertical.

The equivalent mass and equivalent mass MOI are inversely proportional to the modal displacement of the structural vibration mode. Among all modes, the minimum vertical equivalent mass (i.e., the maximum vertical vector amplitude of structural vibration mode) should be selected as the vertical bending design mode, and the equivalent mass MOI is also selected in this way. Basically, only the equivalent mass and the equivalent mass MOI corresponding to the first-order vertical bending mode and the first-order torsion mode of the girder are concerned. A pair of symmetrical or anti-symmetrical vertical bending and torsion modes with lower frequencies is usually selected. In this study, the equivalent mass of the first-order anti-symmetrical vertical bending mode (A-V-1) and the equivalent mass MOI of the first-order anti-symmetrical torsion mode (A-T-1) are used for the wind tunnel model design. The relevant values have been bolded in Table 2.

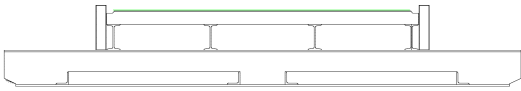
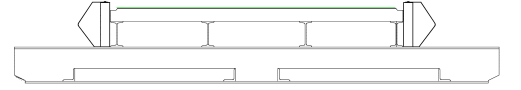
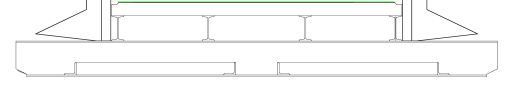
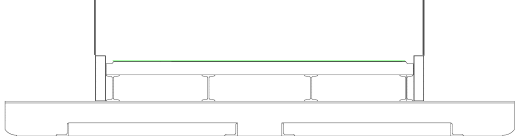
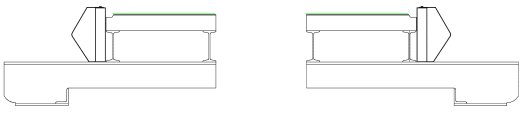
3.3. Aerodynamic Measures and Wind Tunnel Tests

Wind tunnel tests of the girder model are carried out in the CA-1 wind tunnel laboratory of Chang'an University, China. The CA-1 wind tunnel is a return-flow wind tunnel with a test section length of 15 m, height of 3 m, and width of 2.5 m, and the maximum test wind velocity can reach 53 m/s.

3.3.1. Aerodynamic Measures and Girder Model Geometric Design

In order to study the wind-induced vibration response of different aerodynamic sections, seven types of aerodynamic sections are proposed: one basic section, four single measure sections, and two combined measures sections. The specific conditions of the seven measures are shown in Table 3.

Table 3. General information of seven aerodynamic measures for the girder.

Section No.	Girder Configurations	Cross-Section Sketch	Characteristic Description
1	basic section		without aerodynamic design
2	small wind fairing		0.18 m wide and 0.35 m high
3	big wind fairing		0.55 m wide and 0.35 m high
4	central slot		central slotting width 0.80 m
5	wind-retaining plate		the height is 0.50 m
6	small wind fairing + central slot		measure 2 + measure 4
7	big wind fairing + central slot		measure 3 + measure 4

In order to reduce the Reynolds number effects, the test model geometric size should be large enough. On the contrary, the model size should be as small as possible in order to reduce the blockage effects. Considering the wind tunnel test blockage and Reynolds number effects, the model is designed with a geometric scaling ratio of 1:14, a total height of 0.170 m, a full width of 0.286 m, and a full length of 0.866 m. The wind velocity ratio is 1:3, therefore, the Reynolds number of the real bridge is only 42 times of the model Reynolds number, which is only one order of magnitude difference. The actual blockage rate of the test model plus the support system is about 4.5%, which minimizes the blockage effects of the test section. Furthermore, two elliptical thin flat plates are fixed at both ends of the model to ensure the two-dimensional flow characteristics.

3.3.2. Flutter Wind Tunnel Test Design

The dynamic characteristics of the first-order anti-symmetrical vertical bending and torsion mode are selected as the design values of the model. The measured mass errors of the model are less than 1%; the measured frequency errors of the model are less than 2%; the measured damping ratios of the model are close to 0.5%. The parameters of the flutter wind tunnel test model are shown in Table 4.

Table 4. Design and measured parameters of flutter wind tunnel test model.

	Mass (kg)	Mass MOI (kg * m ²)	Vertical Bending Frequency (Hz)	Torsion Frequency (Hz)	Vertical Damping Ratio	Torsional Damping Ratio
Design value	8.426	0.126	1.204	2.343	0.5%	0.5%
Measured value	8.485	0.127	1.222	2.312	0.48%	0.47%
Error	+0.7%	+0.9%	+1.5%	−1.3%	−4%	−6%

The flutter tests are conducted in a uniform wind field with measured turbulence intensity $<0.5\%$ at room temperature (approximately $25\text{ }^{\circ}\text{C}$), with a wind velocity range of 2 m/s to 20 m/s , and a wind attack angle of -5° , -3° , 0° , $+3^{\circ}$, and $+5^{\circ}$. The flutter measurement model is suspended by 8 springs from the steel frame in the wind tunnel, as can be seen in the Figure 4. The basic section model flutter test is shown in Figure 5.

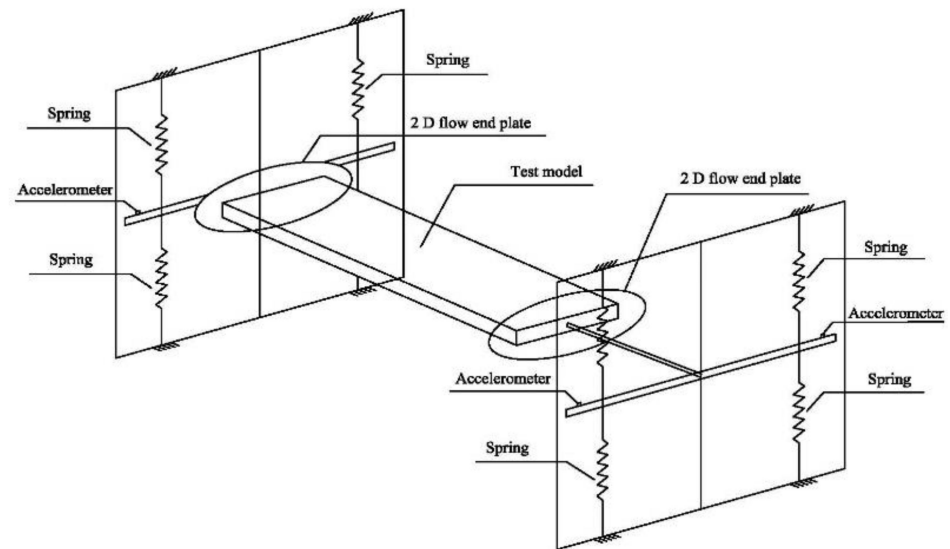


Figure 4. Sketch of the model vibration measurement system.



Figure 5. The basic section model in the CA-1 wind tunnel.

4. Flutter Response and Its Aerodynamic Measures

4.1. Critical Flutter Wind Velocities of Seven Aerodynamic Sections

The flutter response of seven kinds of aerodynamic sections is investigated through wind tunnel tests, and the results of critical flutter wind velocity of various sections are shown in Table 5.

Table 5. Critical flutter wind velocities for various aerodynamic measures (m/s).

Section No.	Girder Configurations	−5° Angle of Attack	−3° Angle of Attack	0° Angle of Attack	+3° Angle of Attack	+5° Angle of Attack
1	basic section	>60	>60	>60	>60	>60
2	small wind fairing	>60	>60	>60	>60	>60
3	big wind fairing	>60	>60	>60	42.6	39.6
4	central slot	>60	>60	>60	>60	>60
5	wind-retaining plate	26.1	29.1	>60	>60	>60
6	small wind fairing + central slot	>60	>60	>60	>60	>60
7	big wind fairing + central slot	>60	>60	>60	>60	>60

Except for Section 3 (big wind fairing) and Section 5 (wind-retaining plate), the critical flutter wind velocities of the other sections are greater than the flutter checking wind velocity of 56.7 m/s. The flutter stability of the big wind fairing section and the wind-retaining plate section is relatively low, the relevant critical flutter wind velocities have been bolded in Table 5. The critical flutter wind velocities of the big wind fairing section at +3° and +5° angles of attack are 42.6 m/s and 39.6 m/s, respectively; the critical flutter wind velocities of the wind-retaining plate section at −3° and −5° angles of attack are 29.1 m/s and 26.1 m/s, respectively.

It also should be noted that the wind-retaining plate can be seen as to seal the bottom of the railing meshwork. When severe cold winter comes, railing meshwork covered snow and ice may form a flow barrier like real wind-retaining plate, and at this time one needs to pay attention to the timely removal of snow and ice to ensure wind-resistant stability.

4.2. Analysis of Soft Flutter Characteristics

The “soft flutter” phenomenon is found to be obvious in the wind tunnel tests of the big wind fairing section and the wind-retaining plate section.

In this section, the sampling frequency for all flutter tests is set to 1000 Hz. The soft flutter response is analyzed by time history analysis and Fourier spectrum analysis.

4.2.1. The Difference between Soft flutter and Hard flutter

Most long-span bridges suffer from “hard flutter”. However, not all of bridge flutter is as linear theory predicts as the amplitude shows exponential growth and instantaneous damage, i.e., “hard flutter”, some of bridge flutter is stabilized to a finite amplitude due to the nonlinear effects of self-excited forces, i.e., a nonlinear “soft flutter” phenomenon. The soft flutter phenomenon has no obvious critical flutter wind velocity, and the flutter divergence has been in a slow development process. The theory of Scanlan linear self-excited forces cannot explain the phenomenon of soft flutter, which generally needs a nonlinear theory of flutter self-excited forces to explain.

It is difficult to summarize which type of bridge section will have soft flutter. The soft flutter phenomenon is highly likely to occur in bluff body II-shaped and H-shaped girder sections [34–37], and some studies have shown that the soft flutter phenomenon also occurs in the box girder sections [38] and even in thin flat sections [39].

The classical Scanlan linear self-excited forces theory, for which the expressions are listed in Equations (3) and (4) below [40,41], treats bridge flutter as a linear aerodynamic instability phenomenon.

$$L_{se} = \frac{1}{2}\rho U^2 B \left[KH_1^*(K) \frac{\dot{h}}{U} + KH_2^*(K) \frac{B\dot{\alpha}}{U} + K^2 H_3^*(K) \alpha + K^2 H_4^*(K) \frac{h}{B} \right] \quad (3)$$

$$M_{se} = \frac{1}{2}\rho U^2 B^2 \left[KA_1^*(K) \frac{\dot{h}}{U} + KA_2^*(K) \frac{B\dot{\alpha}}{U} + K^2 A_3^*(K) \alpha + K^2 A_4^*(K) \frac{h}{B} \right] \quad (4)$$

In Equations (3) and (4), only valid for simple harmonic motion of the girder deck, the self-excited lift force L_{se} and the self-excited torsion moment M_{se} are measured as quantities per unit deck length on a section model. ρ is the air density, U the mean wind velocity perpendicular to the bridge model's axis, B is the deck width; the quantities h and α are the instantaneous vertical motion and torsional angle of the deck section; the over-dot symbol denotes derivation with respect to time t ; the quantities $H_i^*(K)$ and $A_i^*(K)$ (with $i = 1, \dots, 4$) are the flutter derivatives that depend on reduced frequency $K = \omega B/U$, with $\omega = 2\pi f$ being the angular frequency of the deck vibration (rad/s) and f the frequency in Hz.

4.2.2. Soft Flutter of the Big Wind Fairing Section

From the wind tunnel test results, it is shown that the flutter stability of the positive angles of attack of big wind fairing section is not satisfied. Compared with $+3^\circ$ angle of attack, $+5^\circ$ angle of attack has lower flutter stability and larger stable amplitude at the same wind velocity. The flutter velocity of $+5^\circ$ angle of attack is 39.6 m/s, and the wind velocity range of the stable amplitude is 39.6 m/s to 46.2 m/s. The flutter velocity of $+3^\circ$ angle of attack is 42.6 m/s, and the wind velocity range of the stable amplitude is 42.6 m/s to 49.5 m/s.

At the beginning, the torsional amplitude of the big wind fairing section is approximately linearly decreasing, and gradually grows to a stable amplitude (GTS), then the stable amplitude no longer decreases. As the wind velocity increases, the torsional amplitude increases slowly and gradually decrease to a stable amplitude (DTS), and then the stable amplitude no longer increases. As the wind velocity continues to increase, the torsional amplitude approximately linearly grows to divergence amplitude (GTD), and there is no obvious flutter threshold, showing the phenomenon of soft flutter (see Figure 6).

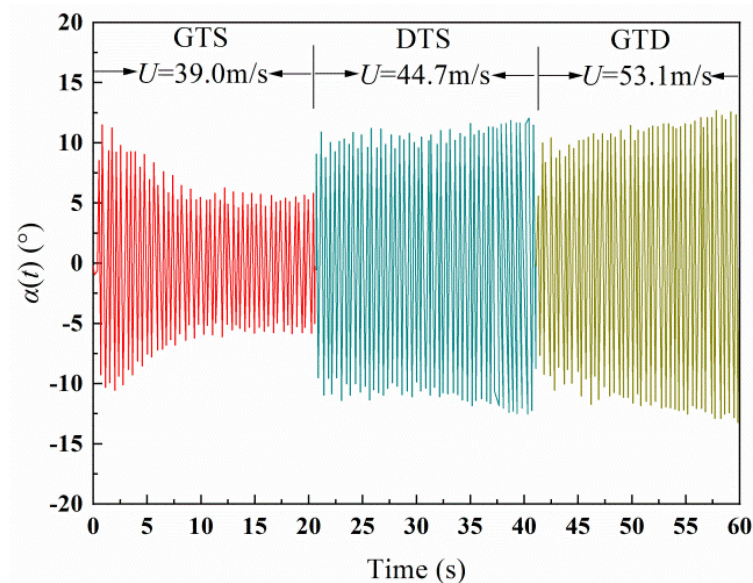


Figure 6. Soft flutter phenomenon of the big wind fairing section, $+5^\circ$ angle of attack.

For further study of the soft flutter of the big wind fairing section, the RMS of the torsional and the vertical displacements at $+5^\circ$ angle of attack are plotted in Figure 7. The vertical and torsional displacements are nondimensionalized. The vertical displacement is divided by the girder width, and the torsional displacement is converted to the radian unit system. From Figure 7, it can be seen that the soft flutter of the big wind fairing section is dominated by the torsional vibration, and the vertical vibration displacement is relatively small. The soft flutter exhibits a vibration pattern with coupled bending and torsional degrees of freedom.

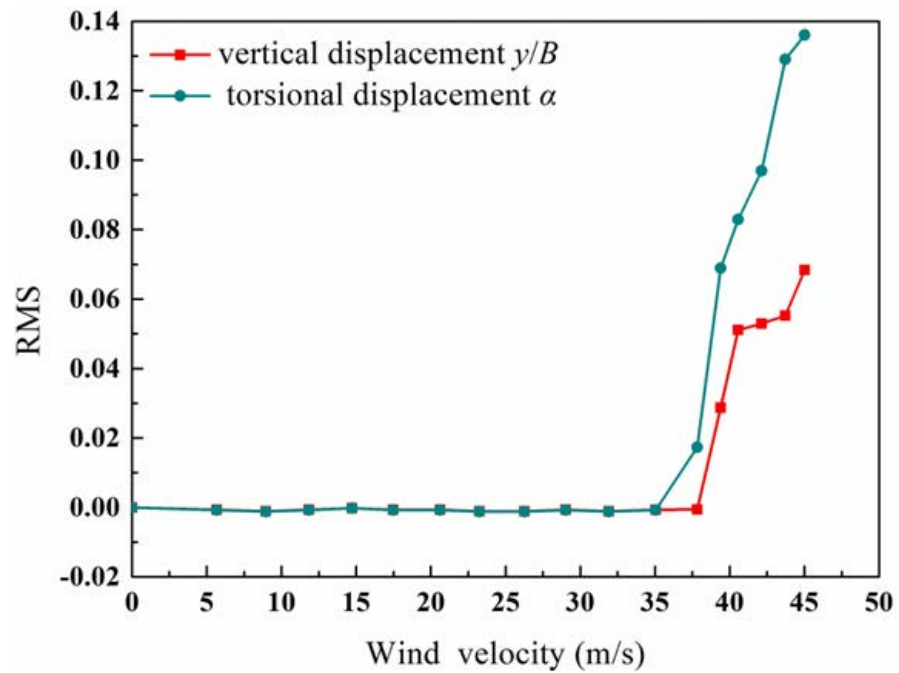


Figure 7. Nondimensionalized RMS displacements of the big wind fairing section, +5° angle of attack.

Figure 8 shows the time histories of the torsional and the vertical displacements at wind velocity $U = 44.7$ m/s and their Fourier spectrum analysis. It can be found that the soft flutter amplitude of the section is dominated by the torsional vibration, and the stable vertical amplitude is only about 2 cm. In the Fourier analysis, there is only one torsional vibration frequency, which is the model torsional frequency, however, the vertical vibration spectrum contains multiple vibration frequencies, and these vertical vibration frequencies approximately present a multiplicative relationship. Each flutter derivative of Scanlan linear self-excited forces is a function of a single frequency rather than multiple frequencies, so the presence of multiple frequency components in Figure 8d makes the Scanlan equations [40,41] no longer valid, and the self-excited forces may be modified by the higher order frequency terms.

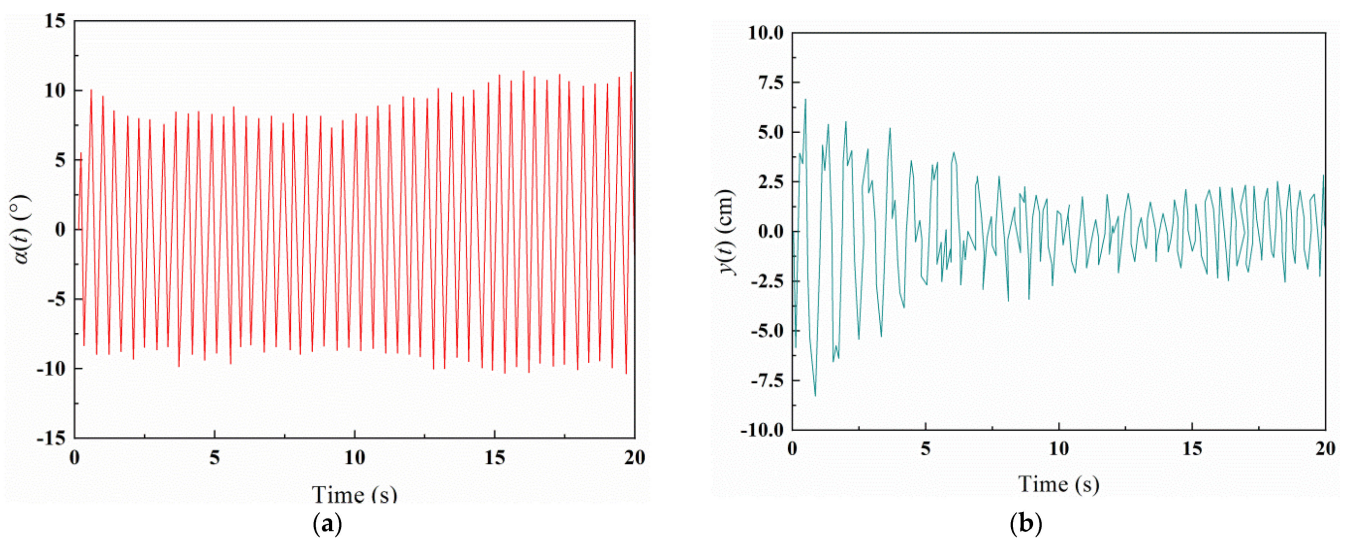


Figure 8. Cont.

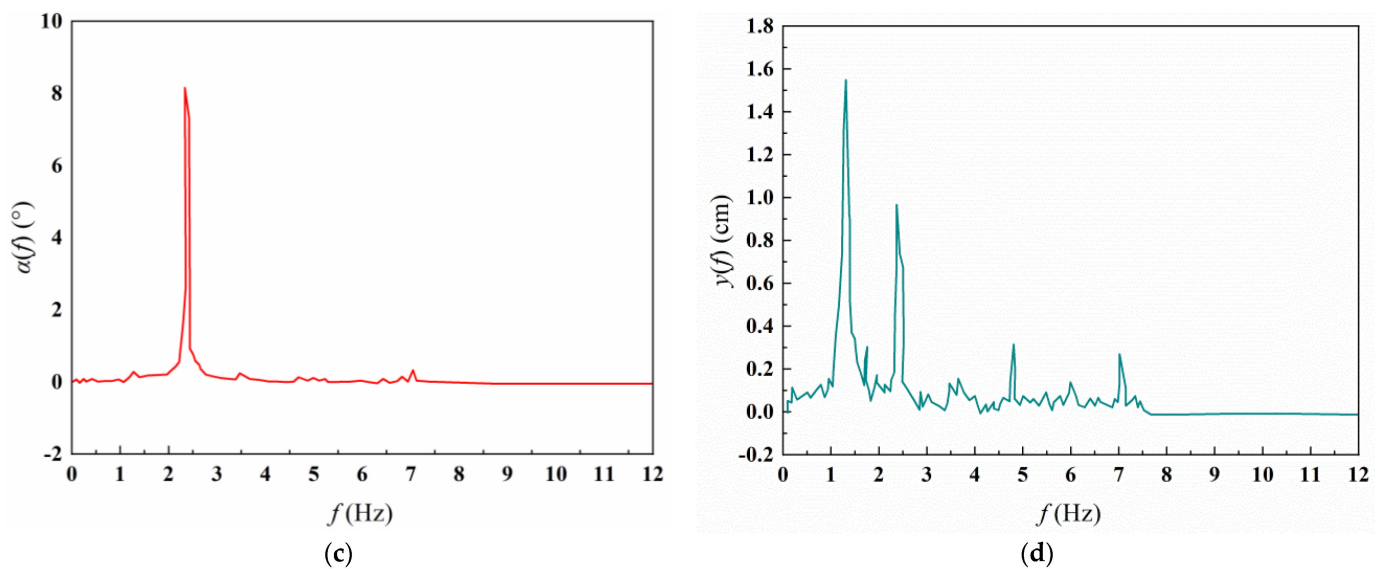


Figure 8. Time histories and frequency spectra of the torsional and the vertical vibration of the big wind fairing section, $+5^\circ$ angle of attack, $U = 44.7$ m/s: (a) Torsional displacement time history; (b) Vertical displacement time history; (c) Torsional displacement spectrum; (d) Vertical displacement spectrum.

4.2.3. Soft Flutter of the Wind-Retaining Plate Section

From the wind tunnel test results, the flutter stability of the negative angles of attack of the wind-retaining plate section is relatively low and cannot satisfy the wind-resistant safety. The starting flutter velocity of the wind-retaining plate section at -5° angle of attack (26.1 m/s) is lower than that of -3° angle of attack (29.1 m/s), and the stable amplitude of -5° angle of attack is larger than that of -3° angle of attack at the same wind velocity. The wind velocity range of the stable amplitude is 26.1 m/s to 31.8 m/s at -5° angle of attack, 29.1 m/s to 52.2 m/s at -3° angle of attack.

No obvious GTS and DTS phenomena are found during the soft flutter, and GTD phenomenon appears when the wind velocity reaches a certain value. There is also a wind velocity range of the stable amplitude between the starting flutter and the divergence. The soft flutter phenomenon of the wind-retaining plate section at -5° angle of attack is shown in Figure 9.

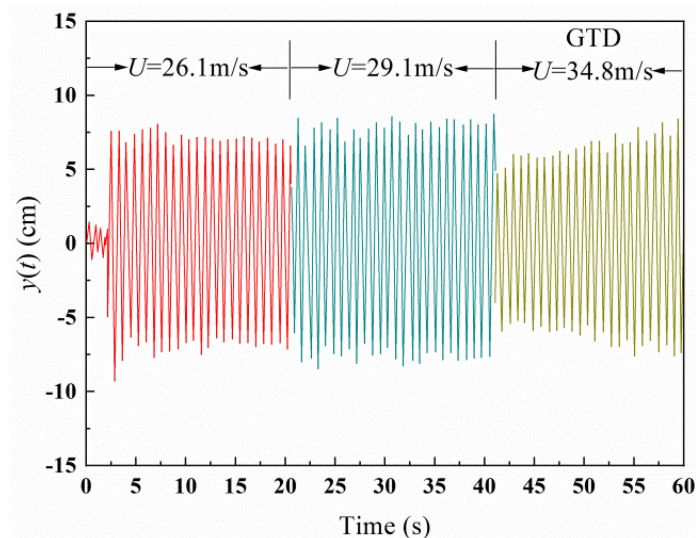


Figure 9. Soft flutter phenomenon of the wind-retaining plate section, -5° angle of attack.

For further analysis of the soft flutter of the wind-retaining plate section, the nondimensionalized RMS of the torsional and the vertical displacements at $+5^\circ$ angle of attack are plotted in Figure 10. From Figure 10, it can be seen that the soft flutter of the wind-retaining plate section is dominated by the vertical vibration, and the torsional vibration displacement is relatively small. The wind-retaining plate section has lower bending and torsional coupling than the big wind fairing section during soft flutter.

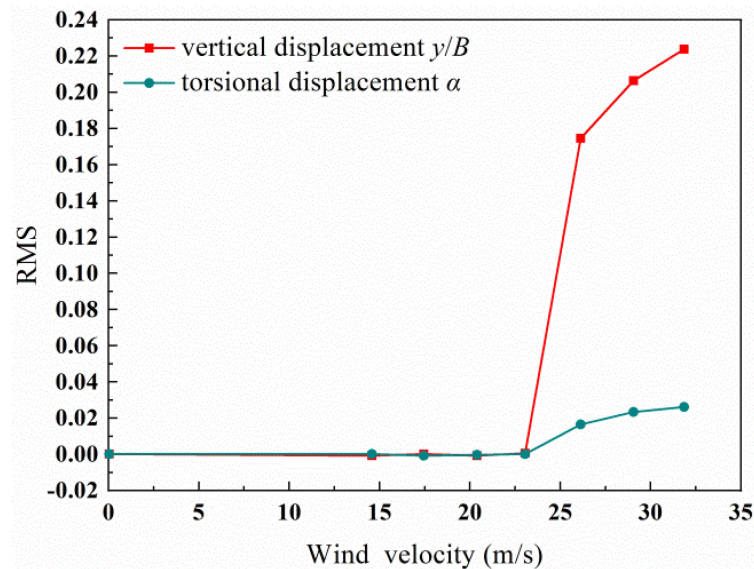


Figure 10. Nondimensionalized RMS displacements of the wind-retaining plate section, -5° angle of attack.

Figure 11 shows the time histories of the torsional and the vertical displacements at wind velocity $U = 29.1$ m/s and their Fourier spectrum analysis. From Figure 11, it can be seen that the torsional displacement is small during the soft flutter, and its stable amplitude is around 1.5° . Fourier spectrum analysis shows that the frequencies of the torsional and the vertical vibration are single, both are the model vibration frequencies, and no multiplicative frequency components are found in the amplitude spectra of the torsional and the vertical vibrations.

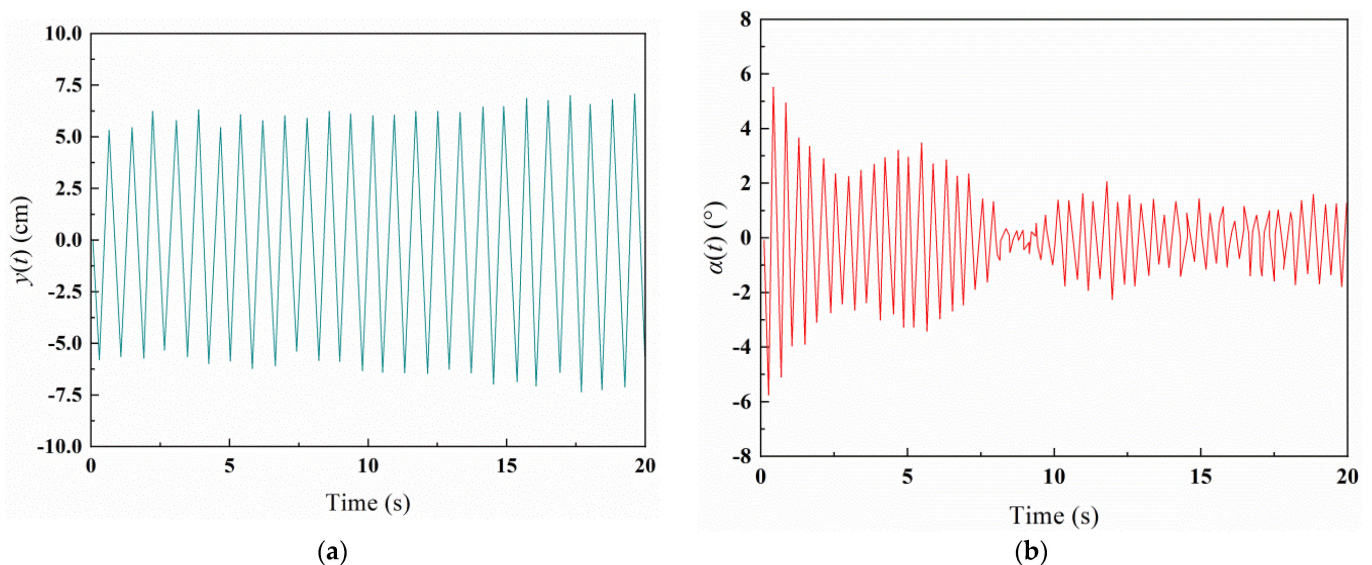


Figure 11. Cont.

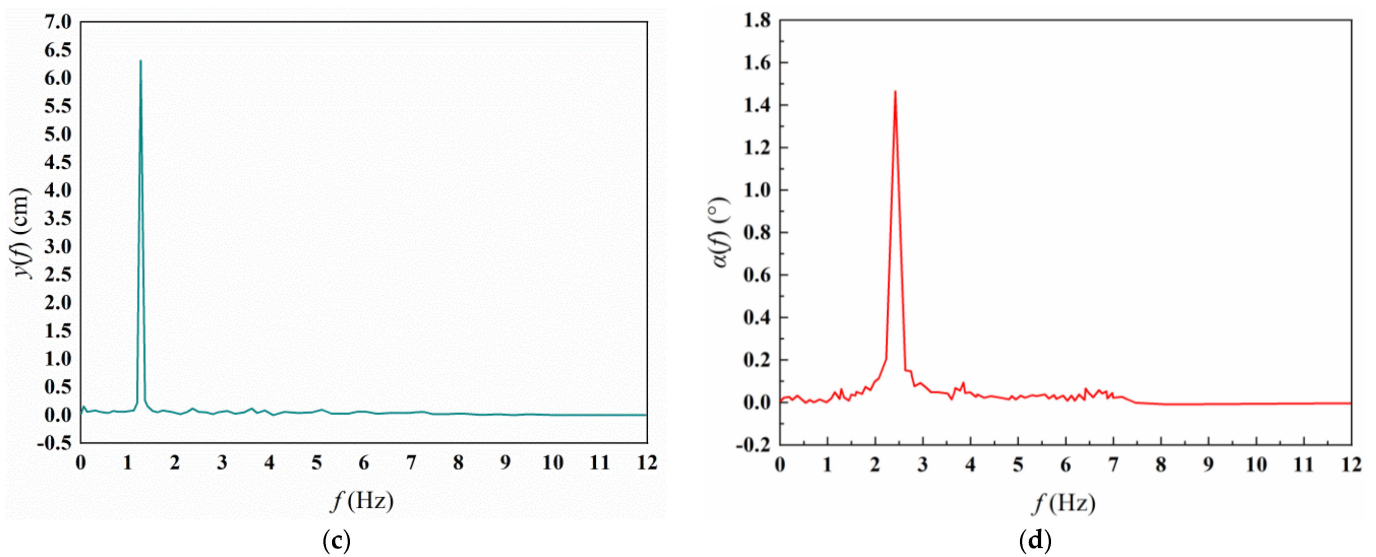


Figure 11. Time histories and frequency spectra of the vibration of the wind-retaining plate section, -5° angle of attack, $U = 29.1$ m/s: (a) Vertical displacement time history; (b) Torsional displacement time history; (c) Vertical displacement spectrum; (d) Torsional displacement spectrum.

It is worth noting that the time history of the torsional vibration of the wind-retaining plate section exhibits obvious beat vibration phenomenon, as shown in Figure 12. At lower wind velocities, the amplitude of the beat vibration decays with time, and as the wind velocity increases, the beat vibration amplitude gradually increases and stabilizes at a certain amplitude. The torsional vibration signal is involved in frequencies close to the model torsional frequency, and the similar frequencies are generated by airflow separation or vortex shedding, which is the cause of the beat vibration phenomenon of the wind-retaining plate section.

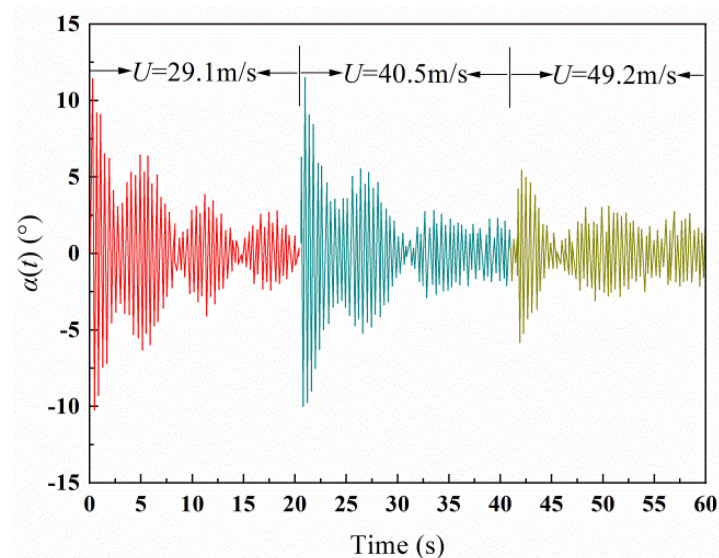


Figure 12. Beat vibration phenomenon of the wind-retaining plate section, -3° angle of attack.

4.3. Discussion of Effective Measures for Flutter Suppression

Through a series of wind tunnel tests, it is found that for the typical bluff body with thin plate-truss structure, the wind fairing measure and the wind-retaining plate measure may not be effective measures to improve the flutter stability. The wind fairing measure will decrease the flutter stability of the positive wind angle of attack, which is prone to soft flutter dominated by the torsional vibration at lower wind velocity. When considering the

use of wind fairing measure, it is necessary to be cautious about the size. Improperly sized wind fairing may cause low wind velocity soft flutter. The wind-retaining plate measure will decrease the flutter stability of the negative wind angle of attack, which is prone to soft flutter dominated by the vertical vibration at lower wind velocity. When the snow on the railing meshwork turns into ice, which significantly affects the ventilation rate of the railing, snow and ice removal work needs to be carried out in time.

Slotting in the center of the girder section can significantly change the flow state of the section, which is an effective measure to improve the flutter stability. Considering the rigidity of the girder and pedestrian comfort, the width of the central slot should not be too large, and it is recommended not to exceed one third of the width of the sidewalk. The combination of the wind fairing and the central slot measures can improve the flutter stability.

5. Conclusions

In the present study, the flutter instability of seven particular aerodynamic measures of the girder section of a 420m-span pedestrian suspension bridge is studied by wind tunnel tests. The time-frequency characteristics of soft flutter of long-span pedestrian suspension bridge are obtained by time history and frequency spectrum analysis. The main conclusions are as follows:

- (1) Wind tunnel tests research shows that for typical bluff body girder with thin plate truss structure, the wind fairing and the wind-retaining plate may be detrimental to flutter stability of long-span pedestrian suspension bridge, the wind fairing will reduce the flutter stability of positive angles of attack and the wind-retaining plate will reduce the flutter stability of negative angles of attack. Central slotting in the girder can significantly change the circumfluence of the section and reduce the airflow vibration energy, which is an effective measure to improve the flutter stability of such girder sections.
- (2) The larger the positive wind angle of attack, the worse the flutter stability of the big wind fairing section. The soft flutter phenomenon of the big wind fairing section is dominated by the torsional vibration with a single frequency, and the vertical vibration is a secondary component. Its vertical vibration spectrum contains multiple frequencies, and these frequencies approximate a multiplicative relationship.
- (3) The larger the negative wind angle of attack, the worse the flutter stability of the wind-retaining plate section. The soft flutter amplitude of the wind-retaining plate is dominated by the vertical vibration of a single frequency, and the frequency multiplication phenomenon is not found in the vertical vibration and the torsional vibration time histories; the torsional vibration time history of the wind-retaining plate section shows obvious beat vibration phenomenon.
- (4) The wind fairing measure increase the width of the girder, which may form alternate vortices on the wake side of the girder section, thus stimulating the soft flutter phenomenon dominated by torsional vibration. The wind-retaining plate measure increase the solid height of the girder, which may form alternate vortices on the upper or lower surfaces of the girder section, thus causing the soft flutter phenomenon dominated by vertical vibration. The traditional Scanlan linear self-excited force theory cannot explain these soft flutter phenomena, so it is necessary to develop nonlinear self-excited force theory.
- (5) This study is a case study of a long-span pedestrian suspension bridge (bridge main span is 420 m, the girder width is 4m, and the width-to-span ratio of the girder section is 1:105), mainly to study the flutter instability of seven particular aerodynamic sections. The findings are only for this type of specific bridge and can provide reference for wind resistance design of long-span pedestrian suspension bridges. For vehicular traffic cable-supported and suspension bridges, a series of case studies is necessary to attain the relevant results.

Author Contributions: Conceptualization, Q.G.; methodology, Q.G. and L.L.; software, Q.G. and L.L.; validation, Q.G., H.G. and J.L.; formal analysis, Q.G. and L.L.; resources, J.L.; data curation, H.G. and Y.W.; writing—original draft preparation, Q.G. and L.L.; writing—review and editing, Q.G.; visualization, L.L. and Y.W.; supervision, Q.G. and H.G.; funding acquisition, Q.G. and J.L. All authors have read and agreed to the published version of the manuscript.

Funding: This research was funded by the Shandong Provincial Natural Science Foundation, grant number ZR2021ME104; the Open Foundation of Key Laboratory of Highway Bridge and Tunnel in Shaanxi Province, grant number 300102219532; the Open Foundation of Tianjin Key Laboratory of Civil Structure Protection and Reinforcement, grant number 12030504; the Tianjin Natural Science Foundation, grant number 18JCQNJC08300; and the Doctoral Research Fund of Shandong Jianzhu University, grant number X20082Z.

Institutional Review Board Statement: Not applicable.

Informed Consent Statement: Not applicable.

Data Availability Statement: The data used to support the findings of this study are available from the corresponding author upon reasonable request.

Conflicts of Interest: The authors declare no conflict of interest.

References

1. Wan, T.B. Key techniques of design of special shape glass floor suspension bridge over Zhangjiajie Grand Canyon. *Bridge Constr.* **2017**, *47*, 6–11. (In Chinese)
2. Guan, Q.H.; Zhou, Y.; Li, J.W.; Hu, Z.T.; Liu, J.X. Effects of parameters on nonlinear aerostatic stability of a pedestrian suspension bridge with main span of 420 m. *J. Vib. Shock* **2018**, *37*, 155–160. (In Chinese) [[CrossRef](#)]
3. Li, Y.; Chen, Z.; Dong, S.J.; Li, J.W. Study on the effects of pedestrians on the aerostatic response of a long-span pedestrian suspension bridge. *KSCE J. Civ. Eng.* **2021**, *25*, 3866–3878. [[CrossRef](#)]
4. Gong, M.; Li, Y.S.; Shen, R.L.; Wei, X.X. Glass suspension footbridge: Human-induced vibration, serviceability evaluation, and vibration mitigation. *J. Bridge Eng.* **2021**, *26*, 05021014. [[CrossRef](#)]
5. Dallard, P.; Fitzpatrick, T.; Flint, A.; Low, A.; Smith, R.R.; Willford, M.; Roche, M. London Millennium Bridge: Pedestrian-induced lateral vibration. *J. Bridge Eng.* **2001**, *6*, 412–417. [[CrossRef](#)]
6. Strogatz, S.H.; Abrams, D.M.; McRobie, A.; Eckhardt, B.; Ott, E. Crowd synchrony on the Millennium Bridge. *Nature* **2005**, *438*, 43–44. [[CrossRef](#)]
7. Blekherman, A.N. Swaying of pedestrian bridges. *J. Bridge Eng.* **2005**, *10*, 142–150. [[CrossRef](#)]
8. Živanović, S.; Pavic, A.; Reynolds, P. Vibration serviceability of footbridges under human-induced excitation: A literature review. *J. Sound Vib.* **2005**, *279*, 1–74. [[CrossRef](#)]
9. Venuti, F.; Bruno, L. Crowd-structure interaction in lively footbridges under synchronous lateral excitation: A literature review. *Phys. Life Rev.* **2009**, *6*, 176–206. [[CrossRef](#)]
10. Pirner, M.; Fischer, O. Experimental analysis of aerodynamic stability of stress-ribbon footbridges. *Wind Struct.* **1999**, *2*, 95–104. [[CrossRef](#)]
11. Tanaka, T.; Yoshimura, T.; Gimsing, N.J.; Mizuta, Y.; Kang, W.-H.; Sudo, M.; Shinohara, T.; Harada, T. A study on improving the design of hybrid stress-ribbon bridges and their aerodynamic stability. *J. Wind Eng. Ind. Aerod.* **2002**, *90*, 1995–2006. [[CrossRef](#)]
12. Stoyanoff, S. A unified approach for 3D stability and time domain response analysis with application of quasi-steady theory. *J. Wind Eng. Ind. Aerod.* **2001**, *89*, 1591–1606. [[CrossRef](#)]
13. Salvatori, L.; Spinelli, P. Effects of structural nonlinearity and along-span wind coherence on suspension bridge aerodynamics: Some numerical simulation results. *J. Wind Eng. Ind. Aerod.* **2006**, *94*, 415–430. [[CrossRef](#)]
14. Taylor, I.J.; Vezza, M.; Salisbury, I. Numerical investigation of the effects of pedestrian barriers on aeroelastic stability of a proposed footbridge. *J. Wind Eng. Ind. Aerod.* **2008**, *96*, 2418–2437. [[CrossRef](#)]
15. Taylor, I.J.; Vezza, M. A numerical investigation into the aerodynamic characteristics and aeroelastic stability of a footbridge. *J. Fluids Struct.* **2009**, *25*, 155–177. [[CrossRef](#)]
16. Rizzo, F.; Caracoglia, L.; Montelpare, S. Predicting the flutter speed of a pedestrian suspension bridge through examination of laboratory experimental errors. *Eng. Struct.* **2018**, *172*, 589–613. [[CrossRef](#)]
17. Lebedev, A.A.; Salenko, S.D.; Obukhovskiy, A.D.; Gosteev, Y.A.; Yashnov, A.N. Aerodynamic investigations of FRP pedestrian suspension bridge span. *AIP Conf. Proc.* **2019**, *2125*, 030053. [[CrossRef](#)]
18. Salenko, S.; Obukhovskiy, A.; Gosteev, Y.; Yashnov, A.; Lebedev, A. Strength, flexural rigidity and aerodynamic stability of fiberglass spans in pedestrian suspension bridge. *Transp. Res. Proc.* **2021**, *54*, 758–767. [[CrossRef](#)]
19. Liu, W.Y.; Tang, H.J.; Yang, X.Y.; Xie, J.M. Improvement of dynamic responses of a pedestrian bridge by utilizing decorative wind chimes. *Wind Struct.* **2020**, *30*, 317–323. [[CrossRef](#)]

20. Qi, D.C.; Chen, X.H.; Zhu, Y.W.; Zhang, Q. A new type of wind-resistance cable net for narrow suspension bridges and wind-resistance cable element for its calculation. *Structures* **2021**, *33*, 4243–4255. [[CrossRef](#)]
21. Tadeu, A.; Marques da Silva, F.; Ramezani, B.; Romero, A.; Škerget, L.; Bandeira, F. Experimental and numerical evaluation of the wind load on the 516 Arouca pedestrian suspension bridge. *J. Wind Eng. Ind. Aerod.* **2022**, *220*, 104837. [[CrossRef](#)]
22. Sato, H.; Hirahara, N.; Fumoto, K.; Hirano, S.; Kusuhara, S. Full aeroelastic model test of a super long-span bridge with slotted box girder. *J. Wind Eng. Ind. Aerod.* **2002**, *90*, 2023–2032. [[CrossRef](#)]
23. Yang, Y.X.; Wu, T.; Ge, Y.J.; Kareem, A. Aerodynamic stabilization mechanism of a twin box girder with various slot widths. *J. Bridge Eng.* **2015**, *20*, 04014067. [[CrossRef](#)]
24. Trein, C.A.; Shirato, H.; Matsumoto, M. On the effects of the gap on the unsteady pressure characteristics of two-box bridge girders. *Eng. Struct.* **2015**, *82*, 121–133. [[CrossRef](#)]
25. Miranda, S.; Patruno, L.; Ricci, M.; Ubertini, F. Numerical study of a twin box bridge deck with increasing gap ratio by using RANS and LES approaches. *Eng. Struct.* **2015**, *99*, 546–558. [[CrossRef](#)]
26. Tang, H.J.; Li, Y.L.; Chen, X.Z.; Shum, K.M.; Liao, H.L. Flutter performance of central-slotted plate at large angles of attack. *Wind Struct.* **2017**, *24*, 447–464. [[CrossRef](#)]
27. Tang, H.J.; Zhang, H.; Mo, W.; Li, Y.L. Flutter performance of box girders with different wind fairings at large angles of attack. *Wind Struct.* **2021**, *32*, 509–520. [[CrossRef](#)]
28. Ma, C.M.; Li, Z.G.; Meng, F.C.; Liao, H.L.; Wang, J.X. Wind-induced vibrations and suppression measures of the Hong Kong-Zhuhai-Macao Bridge. *Wind Struct.* **2021**, *32*, 179–191. [[CrossRef](#)]
29. Greco, F.; Lonetti, P.; Pascuzzo, A. Dynamic analysis of cable-stayed bridges affected by accidental failure mechanisms under moving loads. *Math. Probl. Eng.* **2013**, *2013*, 302706. [[CrossRef](#)]
30. Lonetti, P.; Pascuzzo, A. Design analysis of the optimum configuration of self-anchored cable-stayed suspension bridges. *Struct. Eng. Mech.* **2014**, *51*, 847–866. [[CrossRef](#)]
31. Jiang, C.; Wu, C.; Cai, C.S.; Xiong, W. Fatigue analysis of stay cables on the long-span bridges under combined action of traffic and wind. *Eng. Struct.* **2020**, *207*, 110212. [[CrossRef](#)]
32. Jiang, C.; Wu, C.; Cai, C.S.; Jiang, X.; Xiong, W. Corrosion fatigue analysis of stay cables under combined loads of random traffic and wind. *Engineering Structures. Eng. Struct.* **2020**, *206*, 110153. [[CrossRef](#)]
33. Chen, A.R.; Ma, R.J.; Wang, D.L.; Liu, G.; Ai, H.L.; Liu, T.C. *Wind-Resistant Design Specification for Highway Bridges*; Ministry of Transport of the PRC; China Communications Press: Beijing, China, 2019.
34. Daito, Y.; Matsumoto, M.; Araki, K. Torsional flutter mechanism of two-edge girders for long-span cable-stayed bridge. *J. Wind Eng. Ind. Aerod.* **2002**, *90*, 2127–2141. [[CrossRef](#)]
35. Katsuchi, H.; Yamada, H.; Nishio, M.; Okazaki, Y. Improvement of aerodynamic stability of suspension bridges with H-shaped simplified stiffening girder. *Front. Struct. Civ. Eng.* **2016**, *10*, 93–102. [[CrossRef](#)]
36. Zheng, S.X.; Guo, J.F.; Zhu, J.B.; Tang, Y. Characteristics and suppression measures for soft flutter of main girder with II-shaped cross section. *J. Southwest Jiaotong Univ.* **2017**, *52*, 458–465. (In Chinese) [[CrossRef](#)]
37. Gao, G.Z.; Zhu, L.D.; Han, W.S.; Li, J.W. Nonlinear post-flutter behavior and self-excited force model of a twin-side-girder bridge deck. *J. Wind Eng. Ind. Aerod.* **2018**, *177*, 227–241. [[CrossRef](#)]
38. Zhang, M.J.; Xu, F.Y.; Ying, X.Y. Experimental investigations on the nonlinear torsional flutter of a bridge deck. *J. Bridge Eng.* **2017**, *22*, 04017048. [[CrossRef](#)]
39. Amandolese, X.; Michelin, S.; Choquel, M. Low speed flutter and limit cycle oscillations of a two-degree-of-freedom flat plate in a wind tunnel. *J. Fluids Struct.* **2013**, *43*, 244–255. [[CrossRef](#)]
40. Jain, A.; Jones, N.P.; Scanlan, R.H. Coupled flutter and buffeting analysis of long-span bridges. *J. Struct. Eng.* **1996**, *122*, 716–725. [[CrossRef](#)]
41. Scanlan, R.H.; Jones, N.P.; Singh, L. Inter-relations among flutter derivatives. *J. Wind Eng. Ind. Aerod.* **1997**, *69–71*, 829–837. [[CrossRef](#)]